Catal Lett (2015) 145:1344–1350
DOI 10.1007/s10562-015-1527-2

Flash Synthesis and CO Oxidation of Macro-/Nano-porous Co_3O_4–CeO_2 Via Self-Sustained Decomposition of Metal–Organic Complexes

Dongyang Deng[1] · Nan Chen[1] · Yuxiu Li[1] · Xinxin Xing[1] · Xuechun Xiao[1,2] · Yude Wang[1,2]

Received: 14 January 2015 / Accepted: 4 April 2015 / Published online: 18 April 2015

Abstract Three-dimensional macro/mesoporous Co_3O_4–CeO_2 was prepared via a facile self-sustained decomposition of metal–organic complexes. Porous Co_3O_4–CeO_2 was characterized using X-ray diffraction, scanning electron microscopy/-transmission electron microscopy imaging, N_2 adsorption/desorption and X-ray photoelectron spectroscopy to examine the morphology and microstructure to find out the cause. Co_3O_4–CeO_2 with the 3D hierarchical porous structure consisting of nanoparticles is a coral-like shape with a size of tens of micrometers and exhibits the hierarchically porous morphology, in which the walls of the macropores contain smaller mesopores. The catalytic performance of the porous Co_3O_4–CeO_2 for CO oxidation has been studied. Among the obtained catalysts, the porous Co_3O_4–CeO_2 with 20 wt% Co exhibits the best catalytic activity and the 50 % CO conversion can be reached at 74 °C. The presence of transition metal element Co can promote the production of oxygen vacancies and improve oxygen mobility, which result in enhancing the oxygen-storage capacity of porous Co_3O_4–CeO_2 and its catalytic performance for CO conversion.

Graphical Abstract

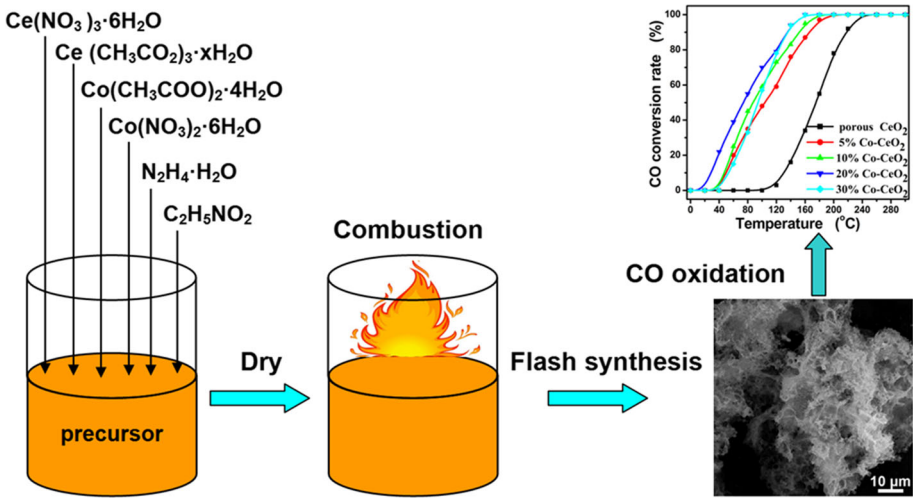

✉ Yude Wang
ydwang@ynu.edu.cn

[1] School of Physical Science and Technology, Yunnan University, Kunming 650091, People's Republic of China

[2] Yunnan Province Key Lab of Micro-Nano Materials and Technology, Yunnan University, Kunming 650091, People's Republic of China

Keywords Porous Co_3O_4–CeO_2 · Flash synthesis · Hierarchical porous structure · Nanocrystalline materials · CO oxidation

1 Introduction

As an excellent catalytic material, cerium dioxide (CeO_2) has been found to be effective in the promotion of catalytic reactions for CO oxidation [1]. The redox and catalytic properties of ceria are dependent upon its oxygen storage and release capacity (OSC) via the redox shift between Ce^{4+} and Ce^{3+} under oxidizing and reducing conditions, respectively [2, 3]. However, the CeO_2 is not a promising candidate for catalytic samples mainly due to its low catalytic activities [4–9]. Numerous reports have shown that the activity of ceria in total oxidation reactions is greatly enhanced by transitional metals like Co, Cu, Ti, Ni, and so on [10–12]. Co_3O_4 is widely used as a non-noble metallic oxide in the catalysis field and shows very high CO oxidation activity in CO/O_2 mixtures even at ambient temperature. As compared with cobalt oxide and ceria catalysts, integrating cobalt oxides with ceria can further enhance the redox behavior for CO [10, 13, 14]. Thus, catalytically active Co and Ce sites in Co_3O_4–CeO_2 composite oxides can cooperatively enhance the catalytic activity [15–20].

The synthesis and preparation of porous Co_3O_4–CeO_2 with desired structure and morphology are of great technological and scientific interests owing to their superior electrochemical performances and catalytic activities. Through increasing surface area, decreasing particle size distribution and preferentially exposing more active lattice planes, the catalytic performance of Co_3O_4–CeO_2 could be optimized. Compared with conventional nanoparticulate system, porous Co_3O_4–CeO_2, possessing the advantages of large surface areas, distinctive structural features and intriguing properties, has attracted much attention in catalysis. The synthesis and preparation of porous Co_3O_4–CeO_2 with desired structure and morphology are of great technological and scientific interests owing to their superior electrochemical performances and catalytic activities. Although great progress has been made, it remains a challenge to synthesize porous Co_3O_4–CeO_2 with controlled morphology and pore size due to the fact that the performance of Co_3O_4–CeO_2 improved by designed porous structure and novel morphology is still undesirable. Therefore, the development of new synthetic routes in order to obtain porous Co_3O_4–CeO_2 material is of a great significance. On the other hand, the porosity of the products prepared by the template-free route is relatively low and the preparation procedure is also multi-step and complex. Herein, we report a rapid and feasible template/surfactant-free route to fabricate a 3D macro-/meso-porous Co_3O_4–CeO_2, which possesses a coral-like shape with a size of tens of micrometers and the hierarchically porous morphology, in which the walls of the macropores contain smaller mesopores. The achieved 3D macro-/meso-porous Co_3O_4–CeO_2 was used as active catalyst for CO oxidation.

2 Experimental

2.1 Chemicals

All chemical reagents used in the experiments were obtained from commercial sources as guaranteed-grade reagents and used without further purification.

2.2 Synthesis of 3D Macro-/Nano-porous Co_3O_4–CeO_2

The synthesis of 3D macro-/nano-porous Co_3O_4–CeO_2 was performed by rapidly heating aqueous solution contains stoichiometric quantity of corresponding metal nitrates and acetates, hydrazine monohydrate ($N_2H_4{\cdot}H_2O$) and glycine ($C_2H_5NO_2$) at a certain temperature (400 °C). Scheme 1 illustrates the synthesis procedure of porous Co_3O_4–CeO_2. In a typical synthesis, $Ce(NO_3)_3{\cdot}6H_2O$, $Ce(CH_3CO_2)_3{\cdot}xH_2O$, $N_2H_4{\cdot}H_2O$, and glycine with a molar ratio (Ce^{3+}:$C_2H_5NO_2$:$N_2H_4{\cdot}H_2O$ = 4:2:1, Co^{2+}/Ce^{3+} = 0, 5, 10, 20, 30 at.%, respectively) were dissolved in deionized water (15 ml) to form a turbid precursor of metal–organic complex. After magnetically stirring for 10 min, the mixture was poured into a crucible and transferred to a preheated furnace at 400 °C. After the elapsed reaction time of 30 min, the crucible was taken out from the furnace and left to cool down spontaneously to the room temperature. The resultant powders were collected and directly subjected to the various characterizations.

2.3 Characterization

Crystal structure of macro-/nano-porous Co_3O_4–CeO_2 was characterized by a Rigaku D/max-3B diffractometer with an incident X-ray wavelength of 1.540 Å (Cu Kα line), scanned from 10° to 90° (2θ) in steps of 0.01°. Scanning electron microscopy (SEM) images were recorded with XL30ESEM-TMP microscope. Transmission electron microscopy (TEM) measurement was performed on a Zeiss EM 912 Ω instrument at an acceleration voltage of 120 kV. X-ray photoelectron spectroscopy (XPS) was carried out at room temperature in ESCALAB 250 system. All XPS spectra were calibrated with reference to C1s peak (285.0 eV) to compensate for the charge effect. The N_2

adsorption–desorption isotherm and pore size distribution curve at 77 K were recorded on a Micromeritics AutoPore IV 9500 system.

2.4 Catalytic Evaluation

The catalytic activity of the Co_3O_4–CeO_2 composites heated in situ for CO oxidation was evaluated at atmospheric pressure in a 50 mg in a glass tubular reactor. The total flow rate of the reaction gas was flow of 30 L h^{-1} g^{-1}, with a 1 % CO and fresh air balanced composition from air generator. The composition of the gas exiting the reactor was monitored by online gas chromatography (GC 9800). The CO conversion (R_{CO}) was calculated from the change in CO concentrations of the inlet and outlet gases as follow:

$$R_{CO} = \left(1 - \frac{[CO]_{out}}{[CO]_{in}}\right) \times 100\,\% \quad (1)$$

where, $[CO]_{in}$ and $[CO]_{out}$ stand for the CO concentrations in the feed gas and effluent gas, respectively.

3 Results and Discussion

X-ray diffraction (XRD) patterns of pure porous CeO_2 and Co_3O_4–CeO_2 are presented in Fig. 1. All the materials are the random orientation with good crystallinity. The present peaks in the spectra confirm the polycrystalline nature of the powders, which were identified to originate from (111), (200), (220) and (311) reflections of cubic CeO_2 crystal structure (JCPDS Card No. 81-0792) and (311) and (440) of Co_3O_4 crystal structure (JCPDS Card No. 42-1467), respectively. From Fig. 1b–d, the XRD patterns of the final products reveal well-developed reflections of CeO_2, without any indication of crystalline byproducts. It also indicates that Co in porous CeO_2 is not as elemental Co or Co compounds, but as impurities in the CeO_2 crystal structure, implying that the Co doping most probably occurs by substituting Ce atom in crystal structure. When the Co content is up to 20 at.% in the reaction system, it can be clearly seen from Fig. 1e, f that all peak positions can be perfectly indexed to CeO_2 and Co_3O_4, respectively. It confirms that the product is a Co_3O_4–CeO_2 mixture and no other impurities were detected.

The morphology of as-prepared material was characterized by SEM. The morphologies of as-prepared porous with the different Co conetents were characterized by SEM and shown in Fig. 2. As shown in Fig. 2, the effects of the different molar ratios of Co on the morphology of macro-/nano-porous can not be observed. The analysis results show the same morphological evolution for the pure CeO_2 and Co_3O_4–CeO_2 with the different Co contents. The as-synthesized powder has a coral-like shape with a size of tens of micrometers, which consists of interconnected spherical particles forming a 3D hierarchical porous structure with typical bimodal porous morphology, in which the walls of the macropores contain smaller mesopores.

TEM investigations give further insight into the morphology and the structural features of the as-synthesized material. TEM image of as-prepared porous 20 %Co–CeO_2 material (Fig. 3a) clearly shows that the 3D hierarchical architecture consists of nanoparticles, the mesopores are formed by the aggregation of nanoparticles and the macropores are self-assembled by nanoparticles, which further confirms SEM deduction. The wall thickness of the macropores is ca. 300–400 nm and the walls consist of many fine nanoparticles. High-resolution TEM (HRTEM) image of porous 20 %Co–CeO_2 are shown in Fig. 3b.The lattice spacing between adjacent planes measured from the observed lattice fringes of HRTEM image is 0.314 nm, corresponding to the distance between (111) crystal planes. The overview images in TEM at low magnification prove

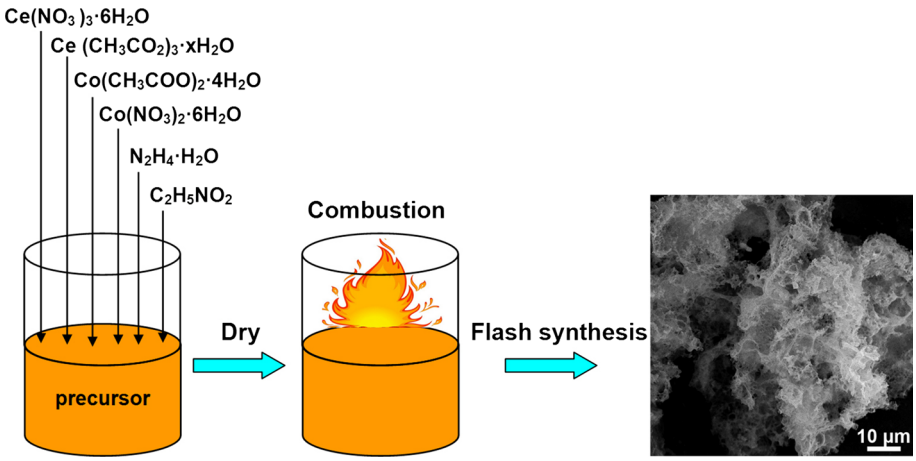

Scheme 1 Synthetic route of macro-/meso-porous Co–CeO_2 materials

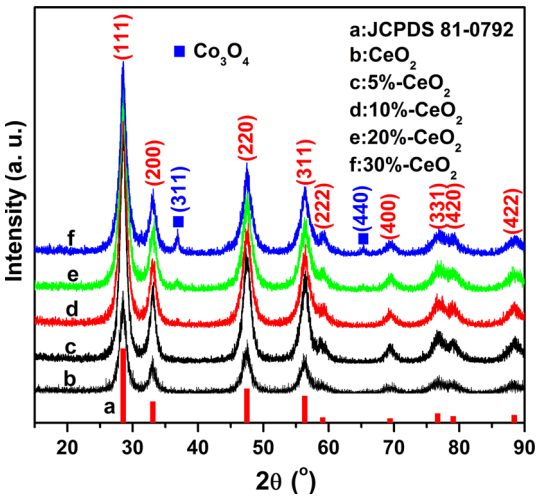

Fig. 1 XRD patterns of the as prepared samples with the different Co contents

that the samples with the different Co contents show the similar 3D hierarchical architecture entirely consisted of individual nanoparticles.

On the basis of the XRD, SEM and TEM results, a possible growth mechanism during the combustion can be speculated. It is well-established that Ce^{3+} can be complexed by $N_2H_4{\cdot}H_2O$, which further precipitates in the presence of anions such as CH_3COO^-. As an oxidizer, NO_3^- can react with $N_2H_4{\cdot}H_2O$. And little glycine is used to induce a relatively intensive combustion reaction. More importantly, the gas evolution from the decomposition of CH_3COO^- during the combustion results in the formation of the porous structure. In the present synthesis process, pores form simultaneously with the CeO_2 lattice formation in one-pot, eliminating the multi-steps of preparation and removal of templates in the commonly used template-assisted approaches. Therefore, the present synthesis route for porous materials is very simple and rapid. A similar process has been reported to generate macro-/meso-porous $ZnCo_2O_4$ [21].

The porous property of the resulting cobalt oxide was further investigated by measuring adsorption–desorption isotherms of nitrogen at 77 K. N_2 adsorption/desorption isotherms and corresponding Barrett–Joyner–Halenda (BJH) pore size distribution plots of the 20 %Co–CeO_2 are shown in Fig. 4. Nitrogen sorption illustrates that nitrogen uptake takes place gradually across the entire adsorption branch of the isotherm indicative of a broad mesopore distribution. Significant hysteresis can be observed between the adsorption and desorption branches followed by the sharp forced closure of the desorption branch, near 0.45 P/P_0, which suggests partial pore blocking. This means that the single nanoparticles within the 3D hierarchical porous structure are not really glued together (already observed in TEM), but are accessible from the outside via a secondary mesopore system. The Brunauer–Emmett–Teller (BET) specific surface area of the as-prepared sample was ca. 56.5 m^2g^{-1}. A broad peak ranging from 2 up to 100 nm can be seen in the pore-size distribution curve (inset of Fig. 4), covering the range of both mesopores and macropores. The pure CeO_2 and Co_3O_4–CeO_2 with the different Co contents show similar specific surface area and pore-size distribution.

To evaluate the potential applicability in catalytic activity for CO oxidation, the catalytic performances of the 3D hierarchical porous Co_3O_4–CeO_2 catalysts in CO oxidation are evaluated under a reaction stream with a gas composition of 1.0 vol% CO balanced by fresh air with 20 vol% O_2. The results obtained for the porous Co_3O_4 and Co_3O_4–CeO_2 catalysts are shown in Fig. 5a, where the CO conversion is reported as a function of temperature. It can be seen that the activity of porous Co–CeO_2 catalysts was greatly enhanced after doping of the Co. The light-off temperature (temperature of 50 % conversion, $T_{50\%}$) of the porous CeO_2 and Co_3O_4–CeO_2 is 175 °C (CeO_2), 104 °C (5 %Co–CeO_2), 87 °C (10 %Co–CeO_2), 50 °C (20 %Co–CeO_2), and 94 °C (30 %Co–CeO_2) from Fig. 5b. The CO conversion of porous 20 %Co–CeO_2 is completed at the temperature of 160 °C, but porous CeO_2 needs a temperature of as high as 240 °C. Among the porous Co_3O_4–CeO_2 catalysts with various Co contents, the 20 %Co–CeO_2 catalyst exhibits the highest catalytic activity at the lowest temperature, as well as the excellent redox capability at the lowest temperature.

Surface compositions and chemical states of the as-synthesized 3D hierarchical porous Co_3O_4–CeO_2 catalysts were carried out by X-ray photoelectron spectroscopy (XPS) to further investigate the mechanism of CO oxidation. The Ce 3d core level peak can be confirmed by XPS analysis, as shown in Fig. 6a. The main features are composed of six peaks corresponding to the three pairs of spin–orbit doublets. Due to its highly non-stoichiometric nature, both valences (3+ and 4+) are presented in CeO_2. The main peaks of Ce^{4+} $3d_{3/2}$ and Ce^{4+} $3d_{5/2}$ are shown at binding energies of ~915.3 and ~897.9 eV, respectively. Those of Ce^{3+} $3d_{3/2}$ and Ce^{3+} $3d_{5/2}$ are located at ~900.5 and ~881.9 eV. Two additional satellite lines SU1 and SU2, which means 'shake-up', are shown at ~906.5 eV on the Ce^{3+} $3d_{3/2}$ and at ~887.5 on the Ce^{3+} $3d_{5/2}$, respectively [22]. The presence of Ce^{3+} is a result of oxygen vacancies and this effect is enhanced in porous structure because a larger fraction of the atoms are on the surface as the particle size is reduced and the surface atoms have reduced coordination. The oxygen vacancies lead to the transformation $Ce^{4+}\leftrightarrow Ce^{3+}$, a key issue in the redox capability of CO. The ratio of Ce^{4+}/Ce^{3+} is 1.14, 1.20, 1.24, 1.39, and 1.30 for porous CeO_2, 5 %Co–CeO_2, 10 %Co–

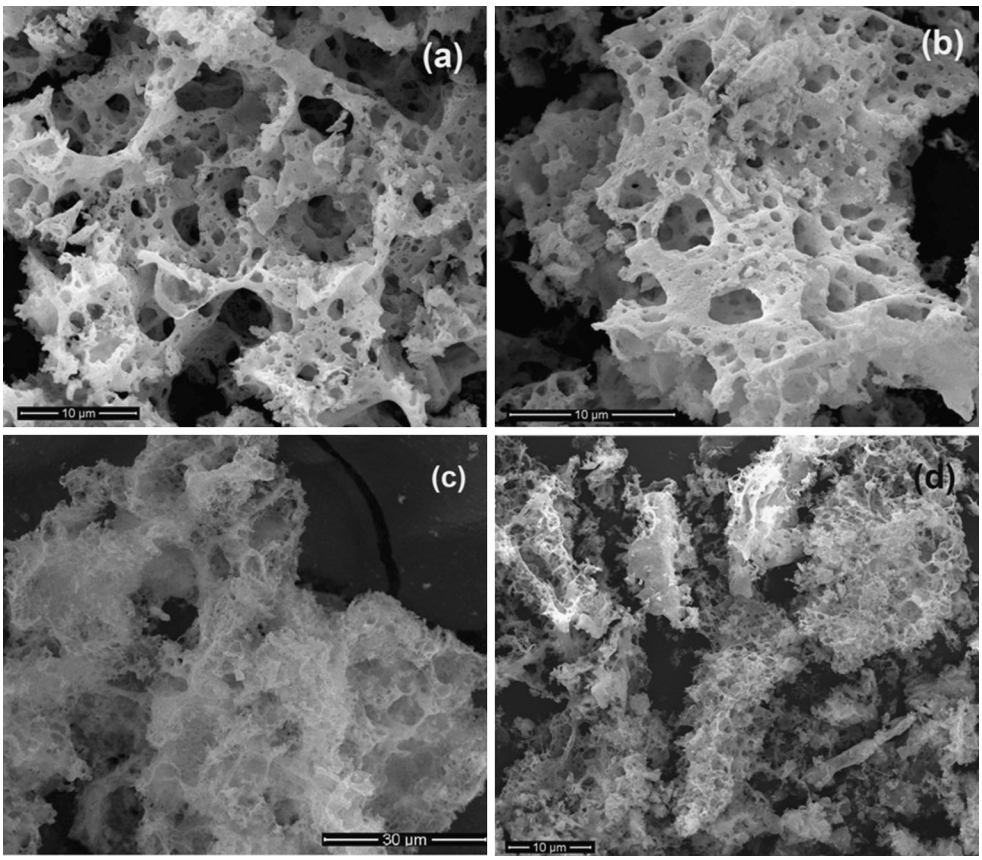

Fig. 2 SEM images of as-prepared samples in the different Co contents. **a** CeO_2, **b** 10 %Co–CeO_2, **c** 20 %Co–CeO_2, and **d** 30%Co–CeO_2

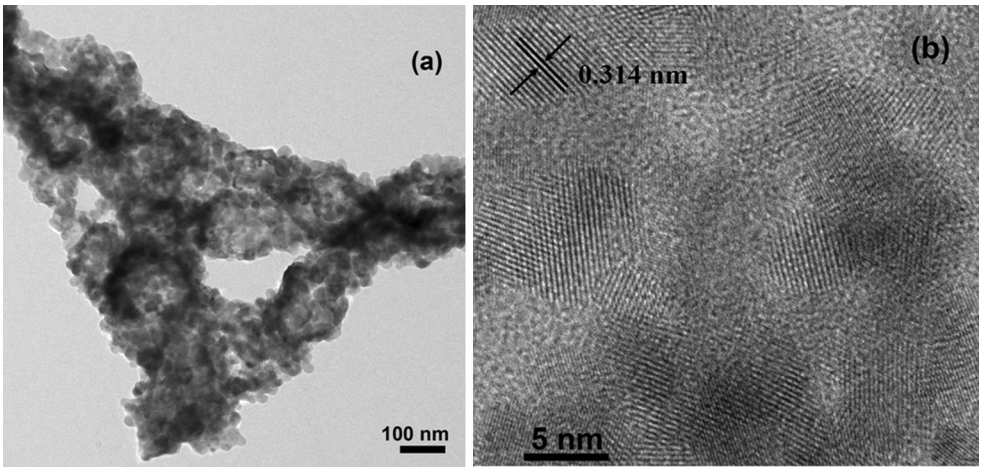

Fig. 3 TEM image (**a**) and HRTEM image (**b**) of 20 %Co–CeO_2 sample

CeO_2, 20 %Co–CeO_2, and 30 %Co–CeO_2, respectively. It is obvious that porous Co–CeO_2 show an increased ratio of Ce^{4+}/Ce^{3+} from XPS findings. As an excellent catalytic material, CeO_2 has a strong oxygen storage and release capacity via the redox shift between Ce^{4+} and Ce^{3+} under oxidizing and reducing conditions, respectively. The Ce^{4+} percentage of 20 %Co–CeO_2 nanoparticles reaches the highest value, indicating the highest redox capacity [23]. The Ce^{4+} percentage of porous 20 %Co–CeO_2 reaches the highest value, indicating the highest redox capacity, which is in good accordance with the CO oxidation reaction results. The XPS results illustrate more oxygen vacancy species in the porous Co–CeO_2. All the spectra show a peak at about 529.4 eV, which is assigned to oxygen ions

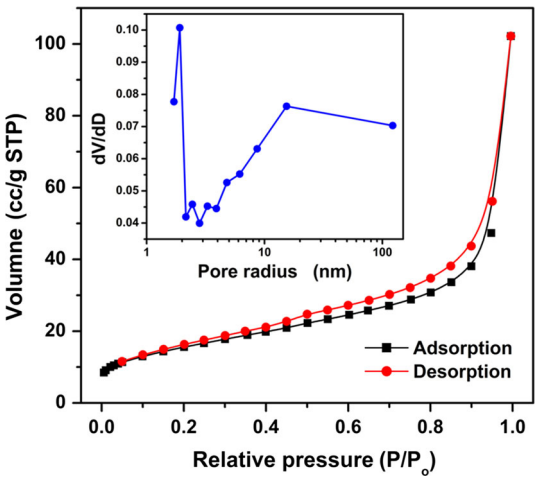

Fig. 4 Nitrogen adsorption and desorption isotherms of 20 %Co–CeO_2 sample with corresponding pore-size distribution (*inset*) calculated by BJH method from desorption

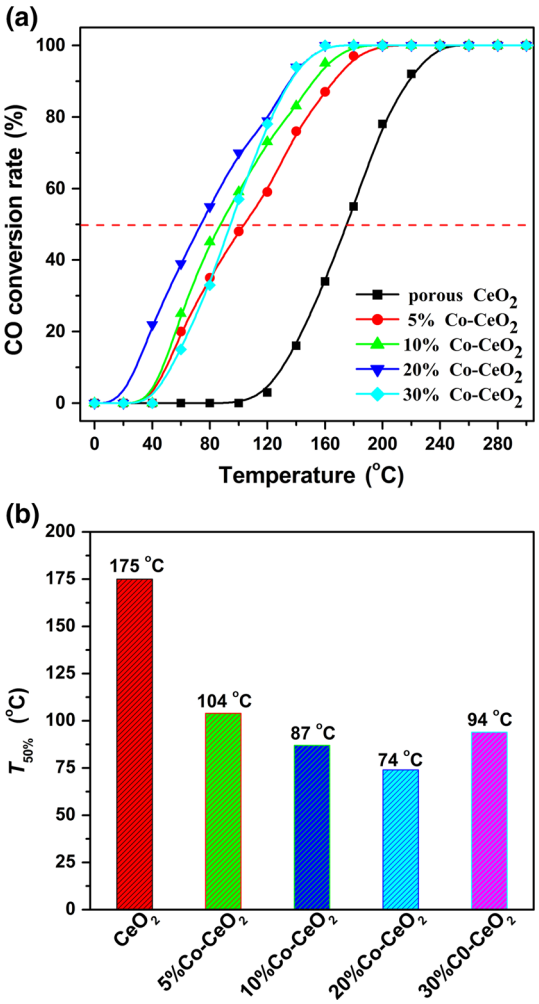

Fig. 5 **a** CO conversion rate as a function of the reaction temperature for various Co–CeO_2 catalysts with the different Co contents. **b** CO oxidation activity on various Co–CeO_2 catalysts at various reaction temperatures

($O_{lattice}$) in CeO_2. Two evident shoulders at higher binding energies at ~531.7 and ~533 eV are present and attributable to oxygen vacancies and hydroxyl groups, respectively. The ratio of oxygen vacancies and hydroxyl groups to $O_{lattice}$ of porous Co–CeO_2 is 0.11, 0.56, .064, 0.78, and 0.61 for porous CeO_2, 5 %Co–CeO_2, 10 %Co–CeO_2, 20 %Co–CeO_2, and 30 %Co–CeO_2, respectively. The ratio is obviously increased, indicating that the content of surface oxygen vacancy and hydroxyl group is increased by composing suitable amounts of Co. However, the surface oxygen vacancy contents would be decreased with further increase the Co contents due to the formation of copper oxide (Co_3O_4) on the surface of nanoparticles. Figure 6b shows the O 1s XPS spectra of the 20 %Co–CeO_2 catalyst. The O 1s peak can be fitted to two kinds of Gaussian peaks. The main peak at 529.3 eV in the O1 s spectrum corresponds to oxygen ions in the crystal lattice (O_{latt}), while the line located at 531.6 eV can be ascribed to the absorbed O_x^- ions (O^- and O_2^- ions) in the oxygen deficient regions within the matrix of CeO_2. The adsorbed oxygen species of O_x^- are known to be active for oxygen exchange and CO oxidation.

The porous 20 %Co–CeO_2 show 100 % conversion of CO at 160 °C. This can be ascribed to the fact that CO strongly adsorbs onto more reduced sites of porous 20 %Co–CeO_2, resulting in less active site for adsorbing surface oxygen O_2, which is activated to O_x^- anion radicals rapidly by oxygen vacancies. The porous 20 %Co–CeO_2 can produce high density of oxygen vacancies, physisorbed and chemisorbed sites for CO, synergic effect between the cycle transition of Ce^{4+}/Ce^{3+}, which are beneficial to the improvement of the catalytic performance. The catalytic performance for CO oxidation is enhanced obviously after being composited with copper. The porous 20 %Co–CeO_2 shows the best activity due to high redox capability and high oxygen vacancy, supported by the XPS analyses results. Based on the discussion above, the possible catalytic mechanism on the porous 20 %Co–CeO_2 is proposed. It is obvious that the ratio of Ce^{4+}/Ce^{3+} and the oxygen vacancy species of porous 20 %Co–CeO_2 increase by composing suitable amounts of Co, indicating that copper induces structure defects and oxygen vacancies as well as perform synergistic effect with cerium ions, which are greatly contributed to the CO oxidation performance [24]. Therefore, the better CO catalytic activity of porous Co_3O_4–CeO_2 can be ascribed to the fact that the porous 20 %Co–CeO_2 can produce high density of oxygen vacancies, physisorbed and chemisorbed sites for CO, synergic effect between the cycle transition of Ce^{4+}/Ce^{3+},

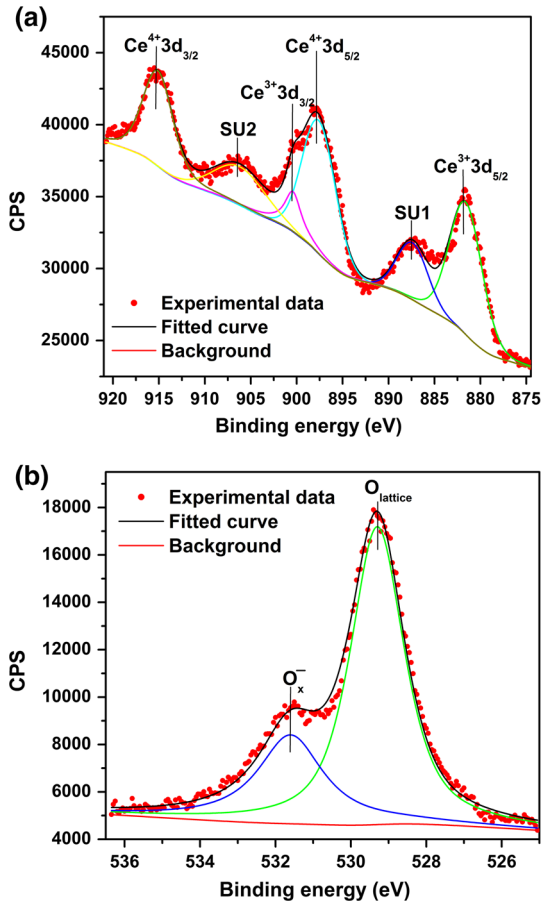

Fig. 6 **a** The high-resolution XPS spectrum of superposed Ce3d for 20 %Co–CeO_2 sample. **b** XPS region spectra of O1s obtained on 20 %Co–CeO_2 sample

which are beneficial to the improvement of the catalytic performance.

4 Conclusion

In summary, 3D macro/mesoporous Co_3O_4–CeO_2 with various Co contents were fabricated by a facile self-sustained decomposition of metal–organic complexes. Porous Co_3O_4–CeO_2 was analyzed by XRD, SEM, TEM, XPS and N_2 adsorption–desorption. The porous Co_3O_4–CeO_2 exhibits 3D hierarchical porous structure with typical bimodal porous morphology, in which the walls of the macropores contain smaller pores. It is suggested that this rapid and feasible template/surfactant-free route is an effective method to fabricate a 3D macro-/nano-porous composite oxides. It is worthwhile to note that the porous Co_3O_4–CeO_2 showed a much higher activity in CO oxidation than porous CeO_2, probably related to the facile redox nature of the cycle transition of Ce^{4+}/Ce^{3+} and the absorbed O_x^- ions of the porous structure.

Acknowledgments This work was supported by National Natural Science Foundation of China (Grant No. 51262029), the Key Project of the Department of Education of Yunnan Province (ZD2013006), Program for Excellent Young Talents, Yunnan University (XT412003) and the Department of Science and Technology of Yunnan Province via the Key Project for the Science and Technology (Grant No. 2011FA001).

References

1. Royer S, Duprez D (2011) ChemCatChem 3:24
2. Hornés A, Hungría B, Bera P, Cámara L, Fernández-García M, Martínez-Arias A, Barrio L, Estrella M, Zhou G, Fonseca JJ, Hanson JC, Rodriguez JA (2010) J Am Chem Soc 132:34
3. Mrabet D, Abassi A, Cherizol R, Do TO (2012) Appl Catal A 447–448:60
4. Jiao Y, Wang FF, Ma XM, Tang QH, Wang K, Guo YM, Yang L (2013) Micropor Mesopor Mater 176:1
5. Shen WH, Dong XP, Zhu YF, Chen HR, Shi JL (2005) Micropor Mesopor Mater 85:157
6. Yang ZJ, Wei JJ, Yang HX, Liu L, Liang H, Yang YZ (2010) Eur J Inorg Chem 2010:3354
7. Xiao GL, Li S, Li H, Chen LQ (2009) Micropor Mesopor Mater 120:426
8. Liang X, Xiao JJ, Chen BH, Li YD (2010) Inorg Chem 49:8188
9. Valentini A, Carreño NLV, Probst LFD, Barison A, Ferreira AG, Leite ER, Longo E (2006) Appl Catal A 310:174
10. Woods MP, Gawade P, Tan B, Ozkan US (2010) Appl Catal B 97:28
11. Liu Y, Wen C, Guo Y, Lu GZ, Wang YQ (2010) J Phys Chem C 114:9889
12. Li TY, Xiang GL, Zhuang J, Wang X (2011) Chem Commun 47:6060
13. Jansson J, Palmqvist AEC, Fridell E, Skoglundh M, Oesterlund L, Thormaehlen P, Langer V (2002) J Catal 211:387
14. Broqvist P, Panas I, Persson H (2002) J Catal 210:198
15. Woods MP, Gawade P, Tan B, Ozkan US (2010) Appl Catal B 97:28
16. Wang H, Zhu H, Qin Z, Wang G, Liang F, Wang J (2008) Catal Commun 9:1487
17. Hou XD, Wang YZ, Zhao YX (2008) Catal Lett 123:321
18. Liu Y, Guo Q (2007) Catal Lett 92:19
19. Tang CW, Kuo CC, Kuo MC, Wang CB, Chien SH (2006) Appl Catal A 309:37
20. Luo JY, Meng M, Zha YQ, Guo LH (2008) J Phys Chem C 112:8694
21. Deng SJ, Han R, Dong CJ, Xiao XC, Wu JM, Wang YD (2014) Mater Lett 134:138
22. Vinodkumar T, Durgasri DN, Reddy BM, Alxneit I (2014) Catal Lett 144:2033
23. Zhang DS, Qian YL, Shi LY, Mai HL, Gao RH, Zhang JP, Yu WJ, Cao WG (2012) Catal Commun 26:164
24. Yao HC, Yao YFY (1984) J Catal 86:254